AGU PUBLICATIONS

JGR

Journal of Geophysical Research: Space Physics

RESEARCH ARTICLE
10.1002/2017JA024606

Key Points:
- The quadrupolar out-of-plane magnetic field associated with reconnection propagates away from the x line as a kinetic Alfvén wave (KAW)
- The attenuation of this KAW is consistent with linear Landau damping theory
- For magnetotail plasma conditions, this KAW can propagate tens of Earth radii with little damping

Correspondence to:
P. Sharma Pyakurel,
psharma@udel.edu

Citation:
Sharma Pyakurel, P., Shay, M. A., Haggerty, C. C., Parashar, T. N., Drake, J. F., Cassak, P. A., & Gary, S. P. (2018). Super-Alfvénic propagation and damping of reconnection onset signatures. *Journal of Geophysical Research: Space Physics*, *123*. https://doi.org/10.1002/2017JA024606

Received 21 JUL 2017
Accepted 28 NOV 2017
Accepted article online 5 DEC 2017

Super-Alfvénic Propagation and Damping of Reconnection Onset Signatures

P. Sharma Pyakurel[1], M. A. Shay[1], C. C. Haggerty[1], T. N. Parashar[1], J. F. Drake[2], P. A. Cassak[3], and S. Peter Gary[4]

[1]Department of Physics and Astronomy, University of Delaware, Newark, DE, USA, [2]University of Maryland, College Park, MD, USA, [3]Department of Physics and Astronomy, West Virginia University, Morgantown, WV, USA, [4]Space Science Institute, Boulder, CO, USA

Abstract The quadrupolar out-of-plane Hall magnetic field generated during collisionless reconnection propagates away from the x line as a kinetic Alfvén wave (KAW). While it has been shown that this KAW carries substantial Poynting flux and propagates super-Alfvenically, how this KAW damps as it propagates away from the x line is not well understood. In this study, this damping is examined using kinetic particle-in-cell simulations of antiparallel symmetric magnetic reconnection in a one-dimensional current sheet equilibrium. In the reconnection simulations, the KAW wave vector has a typical magnitude comparable to an inverse fluid Larmor radius (effectively an inverse ion Larmor radius) and a direction of 85–89° relative to the local magnetic field. We find that the damping of the reconnection KAW is consistent with linear Landau damping results from a numerical Vlasov dispersion solver. This knowledge allows us to generalize our damping predictions to regions in the magnetotail and solar corona where the magnetic geometry can be approximated as a current sheet. For the magnetotail, the KAW from reconnection will not damp away before propagating the approximately 20 Earth radii associated with global magnetotail distances. For the solar corona, on the other hand, these KAWs will completely damp before reaching the distances comparable to the flare loop length.

1. Introduction

Magnetic reconnection plays an important role in plasmas by converting magnetic energy into plasma flows, plasma heating, and energetic particles. The energy converted by magnetic reconnection propagates away from the x line, which is the site where magnetic field lines break and reform. While much of the energy propagates away at MHD speeds, that is, the magnetosonic or Alfvén speed, a significant amount of Poynting flux has been shown to propagate super-Alfvénically in the form of kinetic Alfvén waves (KAWs) associated with the quadrupolar out-of-plane (Hall) magnetic field generated during kinetic reconnection (Lapenta et al., 2013; Shay et al., 2011).

These KAWs are one of the fastest propagating signals generated at the onset of reconnection. Understanding their properties may allow a much more accurate determination of the timing of reconnection onset in observations. As an example, the sudden onset of magnetospheric substorms may be caused by reconnection onset about $20–30R_E$ downtail (Baker et al., 1996) or a near Earth instability around $10R_E$ (Lui, 1996). Determining whether reconnection and/or another instability is initiating substorms requires a careful timing analysis and has been the subject of much scrutiny (Angelopoulos et al., 2008, 2009; Kepko et al., 2009; Lui, 2009; Nishimura et al., 2010). KAWs have been postulated as an energy source for aurora (Lysak & Song, 2004) and have been observed near reconnection sites in the magnetotail (Dai, 2009; Keiling et al., 2003) and during dayside reconnection (Chaston et al., 2005, 2009; Gershman et al., 2017). An important unresolved question is how far these KAWs can propagate before they damp, disperse, or transform into some other wave mode; it is an open question whether these waves generated in the magnetotail make it $20–30\ R_E$ to Earth and generate aurora. A linear analysis of the damping of KAWs in the inner magnetosphere found that most KAWs would be expected to propagate with little damping from $10R_E$ to the ionosphere (Lysak & Lotko, 1996). Mode conversion of compressional waves to KAWs in the strong density gradients of this region can create large parallel electric fields (Lysak & Song, 2011). The morphology of these waves in the inner magnetosphere and auroral zone has been examined with kinetic models, finding both ion (e.g., Chaston et al., 2004) and electron

(e.g., Damiano et al., 2015, 2016; Watt & Rankin, 2009, 2010) energization, either of which may cause aurora. However, the question remains if reconnection-generated KAWs in the more distant magnetotail can successfully transmit significant Poynting flux from a magnetotail x line to the inner magnetosphere.

KAWs in the more distant magnetotail plasma sheet have been modeled using MHD simulations and linear theory (e.g., Lysak & Song, 2004; Lysak et al., 2009). To date, however, a direct fully kinetic study examining both the generation and attenuation of these reconnection-generated KAW has not yet been performed. A first step in this direction is to examine the KAW morphology in the region where the equilibrium geometry can be approximated as a quasi-1D current sheet; this examination is the focus of the current manuscript. The answer to this question can determine if significant reconnection-generated KAW energy can propagate large distances to regions such as the inner magnetosphere, where more complicated global geometry effects due to the Earth's dipole field become important.

To directly examine the damping of KAWs during reconnection, we perform kinetic particle-in-cell (PIC) simulations of antiparallel symmetric reconnection in a 1-D current sheet equilibrium and examine how the structure and amplitude of the Hall field changes as it propagates away from the x line. After being generated, the peak amplitude of the standing KAW structure in the out-of-plane field decreases as it propagates away from the x line. In order to compare with linear Landau damping theory, we estimate the average k for the structure and determine the angle θ between $\mathbf{k}$ and the magnetic field. The reconnection simulations typically have a wave vector $k\,d_s \sim 1$, where $d_s \equiv d_i\,c_s/c_M$ (e.g., Rogers et al., 2001) is the effective fluid Larmor radius, d_i is the ion inertial length, c_s is the sound speed, and c_M is the magnetosonic speed. The angle θ varies between 85° and 89°. We find that the damping of the reconnection KAW is consistent with linear Landau damping predictions from a numerical Vlasov dispersion solver (Gary, 1993).

We emphasize that our findings do not include more complicated geometry effects such as the increase in the magnetic field in the Earth's dipole geometry and at lower altitudes in the solar corona. Modifications to the reconnection generated KAWs due to these effects will be the focus of future studies. With those caveats in mind, we extrapolate the findings to the magnetotail and the solar corona.

Poynting flux from reconnection in the solar corona during solar flares has also been postulated as a mechanism to accelerate electrons and create hard x-rays (Fletcher & Hudson, 2008). Although this previous work has shown that long wavelength Alfvén waves associated with reconnection can drive flows into the solar corona to produce hard x-rays, in our analysis we find that shorter wavelength KAWs associated with reconnection will damp long before they can reach distances comparable to the length of a flare loop; hence, significant energy reaching the photosphere is unlikely.

For the magnetotail, reconnection KAWs with $k\,d_s \sim 1$ ($d_s \approx 0.25 d_i$) can propagate 20 R_E while retaining at least 10% of their initial amplitude. On the other hand, waves with $k\,d_s \gg 1$ are expected to damp completely. Hence, it seems likely that a significant amount of Poynting flux from reconnection-generated KAWs at a near-Earth neutral line may propagate to the inner magnetosphere. Using a simplistic order of magnitude estimate for the amplification of Poynting flux in converging magnetic fields, the predicted Poynting flux magnitude is sufficient to have the potential for generation of aurora.

2. Simulations

For this study, we use the parallel particle-in-cell code P3D (Zeiler et al., 2002) to perform simulations of collisionless antiparallel reconnection in 2.5 dimensions. Calculations are presented in normalized units: the magnetic field to B_0, density to n_0, lengths to ion inertial length c/ω_{pi}, times to inverse ion cyclotron frequency Ω_i^{-1}, temperature to $m_i c_A^2$, and Poynting flux to $S_0 = \frac{c_A B_0^2}{4\pi}$. Using the simulation normalized units, various key physical length scales can be calculated from code values as ion inertial length $d_i = \sqrt{1/n}$; electron inertial length $d_e = \sqrt{(m_e/m_i)\,n}$; ion Larmor radius $\rho_i = \sqrt{T_i}/B$; and electron Larmor radius $\rho_e = \sqrt{T_e\,(m_e/m_i)}/B$. The simulations have a periodic domain with size $L_x \times L_y$ and grid scale Δ. The simulations are initialized with two Harris sheet currents: $B_x = B_{\mathrm{up}}\left(\tanh\left[(y-0.25L_y)/w_0\right] - \tanh\left[(y-0.75L_y)/w_0\right] + 1\right)$ is the equilibrium magnetic field, where w_0 is the half-width of the initial current sheets. The inflowing plasma has magnetic field B_{up} and density n_{up}. A small local magnetic perturbation is added to start the reconnection.

We examine four different simulations, the parameters of which are given in Table 1. Note that the simulations use artificially large m_e/m_i, which is necessary because all electron length and time scales must be resolved in the simulations. The first simulation (sim A) is a high-β simulation. The second (sim B) and third (sim C)

Table 1
Plasma Parameters of Four Simulations : Δ Is Grid Scale, c Is Light Speed, and (L_x, L_y) Are Simulation Domain Sizes

	Simulation parameters											KAW scaling	
Runs	$\frac{m_e}{m_i}$	B_{up}	n_{up}	T_e	T_i	β	c/c_A	$\frac{L_x}{d_i}$	$\frac{L_y}{d_i}$	$\frac{\Delta}{d_i}$	θ	$kd_{i\ell}$	$kd_{s\ell}$
A	0.01	0.3	0.18	0.35	1.2	6.23	30	204.8	102.4	0.025	89	3.88	3.38
B	0.04	1	0.04	9	9	1.44	40	409.6	204.8	0.4	85	1.97	1.27
C	0.04	1	0.04	9	9	1.44	40	1638.4	204.8	0.4	85	1.5	1.0
D	0.04	1	0.2	0.083	0.25	0.13	15	204.8	102.4	0.05	85	3.83	1.0

Note. $d_s = d_i c_s/c_M$ is the effective fluid Larmor radius as described in the text. The subscript "ℓ" denotes the lobe (local) values of parameters used where the KAWs are identified.

have $\beta \sim 1$. Sim C is longer in the x coordinate than the other simulations and allows a direct measurement versus time of the attenuation of the KAW. In the other, shorter simulations, an effective time based on the quasi-steady reconnection rate will be utilized. Lastly, the fourth (sim D) is a low-β simulation.

KAWs in our simulations are identified from the analysis shown in Rogers et al. (2001), where the key controlling length is $d_s \equiv d_i\, c_s/c_M$, and $d_s^2 \gg d_e^2$ is the necessary condition to have KAWs; c_s is the sound speed, and c_M is the magnetosonic speed. Note that for $\beta \ll 1$ this length reduces to $d_s \approx \rho_s = c_s/\Omega_i$, where Ω_i is the ion cyclotron frequency. The angle of propagation and the values of k for each simulation are given in Table 1.

3. Propagation and Damping of KAW

We start by examining the propagation of the magnetic field line after it reconnects and travels downstream. As the magnetic field line reconnects and propagates away from the x line, the magnitude of B_z on the field line grows in time, reaches a peak value, and then begins to decrease in amplitude. For simplicity, we examine times after B_z has reached its peak value.

First, we examine a very long simulation in which the propagation and damping of the KAW can be observed to occur in time, namely sim C. A snapshot of the simulation is shown in Figure 1 at $t = 175\,\Omega_i^{-1}$. B_z and the Poynting flux are enhanced in the exhaust, especially at the outer edges near the separatrices (Figures 1a and 1b). Examining V_{ix} (Figure 1c) reveals significant ion flow that spans the entire domain of the simulation box. The enhanced Poynting flux and quadrupolar structure is due the parallel electron flows near the separatrices that are super-Alfvénic (Shay et al., 2011). The black contour line at the left side of the panels is the field line used to study the morphology of B_z. The evolution of this field line as it propagates away from the x line is shown in Figure 2 on top of the value of B_z in one quadrant of the reconnection region.

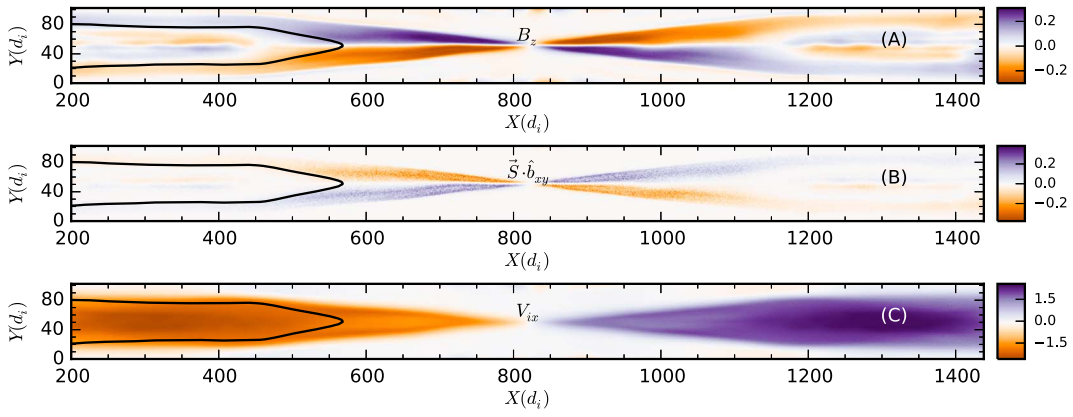

Figure 1. Sim C: At time $t = 175\Omega_i^{-1}$: (a) Out of plane magnetic field B_z, (b) parallel Poynting flux projection onto the x-y plane, and (c) ion outflow velocity V_{ix}. The black contour in all three plots is the magnetic field line tracked to study the KAW propagation. The KAW structure in Figures 1a and 1b broadens significantly and damps as it propagates downstream.

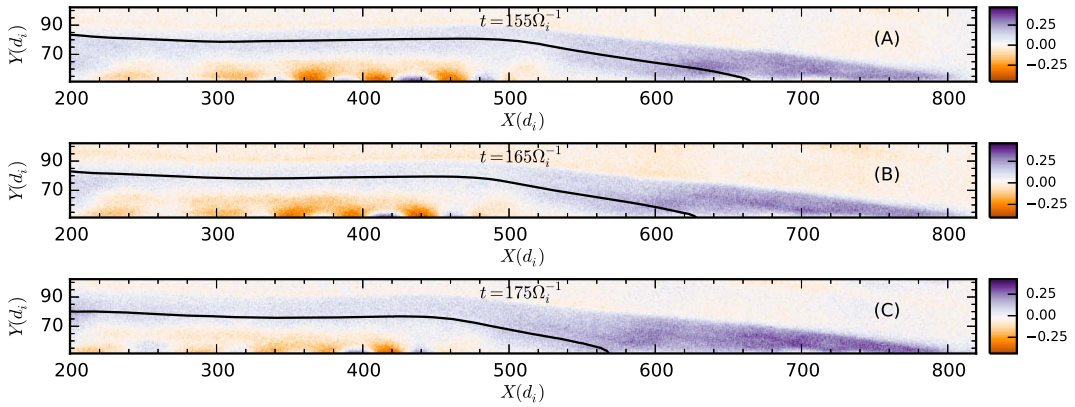

Figure 2. Sim C: Evolution in time of B_z and a single magnetic field line (constant magnetic vector potential ψ).

To examine the propagation and decay of the KAW along this magnetic field, we plot B_z on the field line at different times in Figure 3a. The peak magnitude of B_z steadily decreases in time, and this peak value is plotted versus time in a semilog plot in Figure 3b. The best fit line for an exponential decay is shown, with an exponential decay rate of $1/\tau = 0.0266 \pm 0.0088$.

We have also performed more modest-sized simulations. In these simulations, the reconnection does not proceed long enough to follow a magnetic field as it propagates downstream in the manner of Figure 2. Therefore, for simulations A, B, and D, we use the same analysis methods used in Shay et al. (2011). During the quasi-steady phase of the reconnection simulation, the structure of the KAW in the vicinity of the x line does not change significantly. The motion of the magnetic field lines in this quasi-steady region can be directly linked to the change in magnetic vector potential: $\Delta t = \Delta\psi/E$, where E is the spatially uniform reconnection electric field along the z direction. The effective time difference between magnetic field lines in the exhaust is determined by setting $t = 0$ at the x line, giving $t_{\text{eff}} = (\psi - \psi_{\text{xline}})/E$. In this way, the motion of the magnetic field and the damping of the KAW wave can be studied by examining how B_z changes with changing ψ. An example of this method is shown in Figure 4 for simulation A. The two red and black lines in Figure 4a plotted over the color plot of B_z show the field lines used in this analysis. Note that we only show the first and the last field line, and field lines in between are not shown in Figure 4a. The peak value of B_z on these field lines gradually decreases as the field line propagates away from the x line, as shown in Figure 4b. The change in this peak value with t_{eff} is shown in Figure 4c with a best fit line on a semilog plot. The best fit exponential decay rate is $1/\tau = 0.0237 \pm 0.0049$. Similar analyses were performed for Simulations B and D, yielding $1/\tau = 0.0520 \pm 0.018$ and $1/\tau = 0.0421 \pm 0.0121$, respectively.

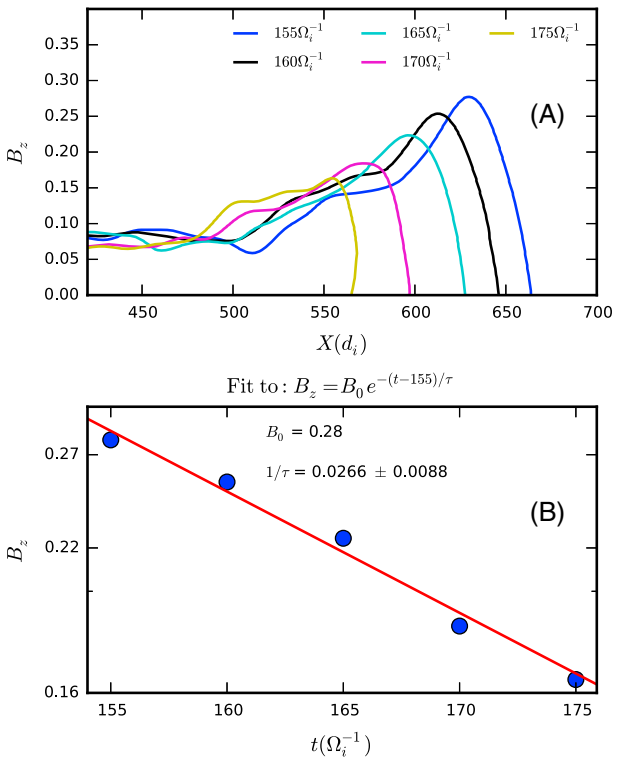

Figure 3. Sim C: (a) B_z along the contours of constant ψ in Figure 2 are plotted at $155\Omega_i^{-1}$, $160\Omega_i^{-1}$, $165\Omega_i^{-1}$, $170\Omega_i^{-1}$, and $175\Omega_i^{-1}$. (b) Peak value of B_z from Figure 3a with respect to time on a semilog scale. The dotted points are simulation data. The red line is the best fit line.

An important question is whether the empirically measured damping rates are consistent with theoretical prediction based on linear Landau resonance. To examine this question, we compare the measured rates to theoretical predictions based on the well-known linear Vlasov dispersion solver (Gary, 1993) that solves the fully electromagnetic plasma dispersion relation using Newton's method. We have compared results of this linear Vlasov solver to the Lysak and Lotko dispersion relation (Lysak & Lotko, 1996); the two show agreement in regimes where the Lysak and Lotko relation is valid (particularly $\beta \ll 1$). The angle of propagation θ relative to the magnetic field is needed to determine the theoretical damping rate. To measure θ, we examine the quasi-1D spatial structure of $\vec{S}\cdot\hat{b}_{xy}$ shown at $t = 175\,\Omega_i^{-1}$ in Figure 5a, where $\vec{S} = \frac{c}{4\pi}\vec{E}\times\vec{B}$ and $\hat{b}_{xy} = (\vec{B}_x + \vec{B}_y)/\sqrt{B_x^2 + B_y^2}$. The green line represents a line of peak value of $\vec{S}\cdot\hat{b}_{xy}$ for the KAW with $\vec{k}$ perpendicular to this line. Clearly, the wave propagation is oblique with $\vec{k}$ nearly perpendicular to the magnetic field. θ is relatively

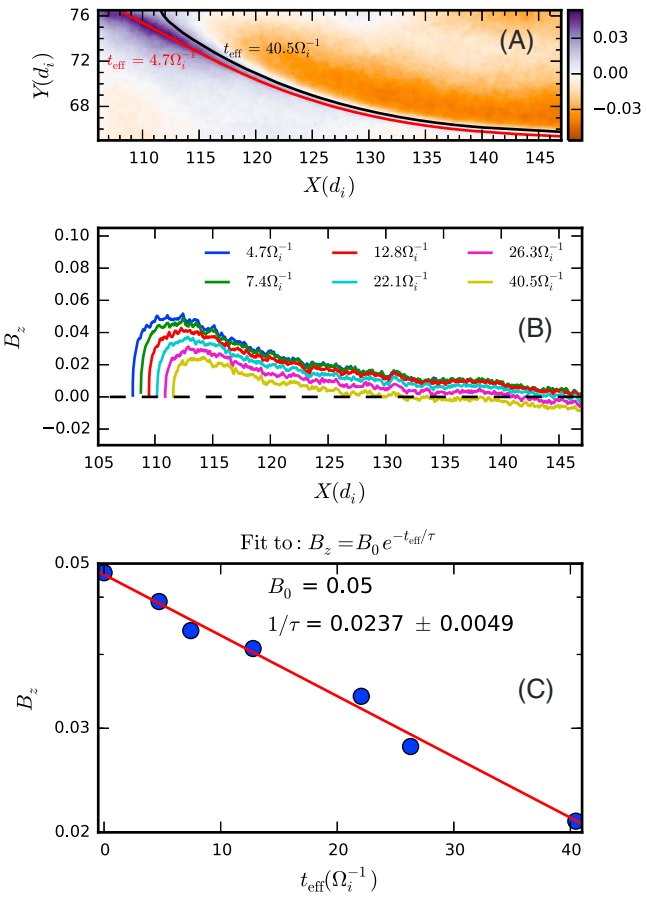

Figure 4. Sim A: (a) lower right quadrant of B_z structure with two magnetic field lines shown as red and black lines with corresponding effective time. (b) B_z along field lines shown in Figure 4a. (c) Peak value of B_z for each field line in Figure 4b with respect to effective time t_{eff} in semilog scale. The quasi-steady reconnection is used to determine t_{eff}, as described in the main body. Best fit line shown in red.

constant for the KAW as shown in Figure 5b, where θ is given versus X along the green line in Figure 5a. We use the average value in Figure 5b of $\theta \approx 85°$ for the linear dispersion solver. In Figure 5c, we determine the magnitude of k by examining $-\vec{S} \cdot \hat{b}_{xy}$ versus the dashed blue line shown in Figure 5a. Half max width is 5.2 giving an approximate wavelength of $\lambda \approx 20.8$ and $k\, d_{s\ell} \approx 1.0$, where $d_{s\ell} = d_{i\ell} c_s / c_m$ is the effective fluid Larmor radius using local values. Note that the local values of the parameters in the vicinity of the KAW that are used for the linear dispersion solver are denoted by the suffix (ℓ). These local values are approximately equal to the inflowing plasma conditions. For each simulation, θ, $k\, d_{s\ell}$, and $k\, d_{i\ell}$ are given in Table 1.

The estimates of θ and k above complete all the parameters required to get the wave frequency and the damping rate, which are B, θ, k, T_e, T_i, and n. We use a well-known Vlasov dispersion solver by Gary (1993) to calculate the frequencies and the damping rates of the KAWs generated in our simulation; note that for each comparison the Vlasov solver uses the same artificial mass ratio as was used in the kinetic PIC simulation.

The comparison between the reconnection findings and Vlasov predictions is shown in Figure 6. The solid lines in the two panels are the linear frequencies from the Vlasov solver (Gary, 1993) using the simulation parameters as inputs. In Figure 6a, the colored circles give the Vlasov real frequencies for the $kd_{i\ell}$ measured in the reconnection simulations. In Figure 6b, the diamonds denote the damping rates measured directly from the reconnection simulations. Highlighting simulation C, the point $(kd_{s\ell}, \frac{\omega_r}{\Omega_i}) = (1.0, 0.1604)$ is the red circle in Figure 6a and the red diamond in Figure 6b is $\frac{\gamma}{\Omega_i} = -0.0266$. The linear Vlasov damping predictions in Figure 6b match the reconnection simulations quite well, even though the simulations do not have a homogeneous background and isotropic temperatures as is assumed in the linear Vlasov dispersion solver. The good agreement between the PIC simulations and linear theory allows us to extrapolate the simulation predictions to realistic parameters in the magnetotail and solar corona in the next section.

One question is whether this damping is due to electron or ion resonance. For simulation D, the parallel KAW speed is a factor of 2 larger than the electron

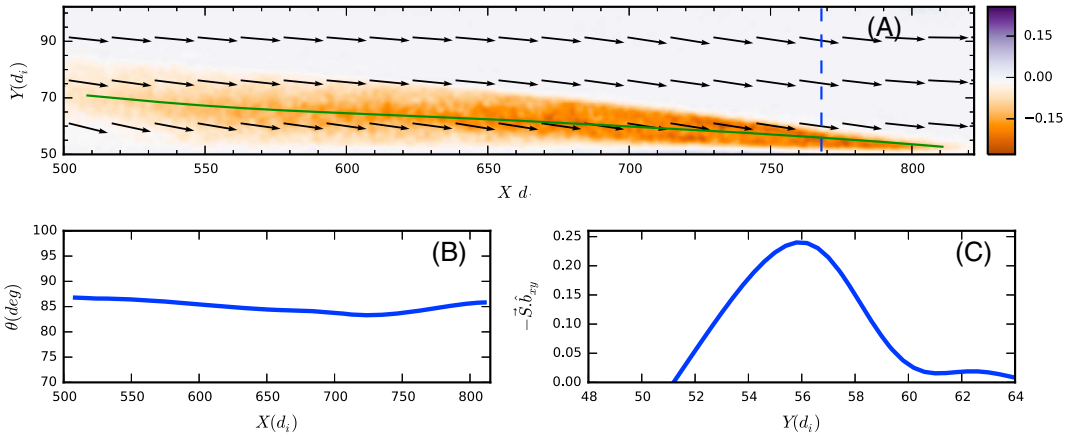

Figure 5. Sim C: Determination of KAW angle of propagation at $t = 175\,\Omega_i^{-1}$. (a) $\vec{S} \cdot \hat{b}_{xy}$ in top left reconnection quadrant with vectors giving magnetic field direction. The green line shows the location of the peak value of the $\vec{S} \cdot \hat{b}_{xy}$ at each x value. The wave vector ($\vec{k}$) is perpendicular to this line. The magnetic field is nearly parallel to the green line, giving a wave vector ($\vec{k}$) that is oblique to the magnetic field. This gives the angle of propagation θ of the KAW that is shown in Figure 5b. (b) θ variation with X along the green line in Figure 5a. (c) $-\vec{S} \cdot \hat{b}_{xy}$ versus the dashed blue line in Figure 5a at $X = 768$. Half max width is 5.2 d_i giving $k\, d_{s\ell} \approx 1.0$ where $d_{s\ell}$ is based on the local density.

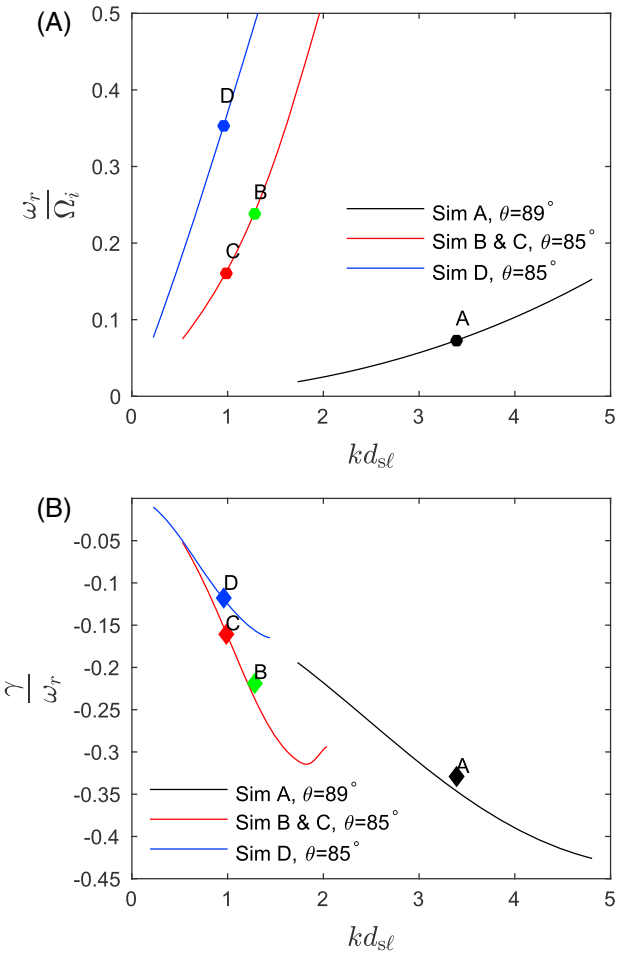

Figure 6. Comparison between Vlasov dispersion predictions and reconnection simulation measurements. The lines show frequencies versus $k\,d_{s\ell}$ from the Vlasov solver. (a) Real frequencies ω_r/Ω_i. The colored circles show the Vlasov solver real frequency at the appropriate $k\,d_{s\ell}$ for each simulation. (b) Damping rates γ/ω_r. The diamonds are measured damping rates for the reconnection simulations at the measured $k\,d_{s\ell}$ value.

thermal velocity and more than a factor of 4 larger than the ion thermal velocity. In simulations A, B, and C, the parallel KAW phase speed lies between the electron and ion thermal velocities and within around a factor of 2 of both of them. However, in this case a parameter sweep using the linear Vlasov solver shows that changing T_e modifies the damping rate substantially. For these reasons, it seems plausible that the damping is due to the electrons.

4. Extrapolation to Magnetotail and Solar Corona Parameters

Ultimately, we wish to determine the fate of the Poynting flux associated with the reconnection KAWs. In the magnetotail, can these KAWs propagate from the reconnection site at $20-30\,R_E$ to the ionosphere and create aurora? Similarly, in the solar corona, could KAWs propagate along a flare loop to the photosphere and create hard x-rays? Using plasma parameters in these two systems, we extrapolate the Landau damping findings to determine the distance traveled before the wave is reduced to 10% its initial amplitude. Note, however, that the direct applicability of these extrapolations is limited to regions where the equilibrium current structure generating reconnection can be approximated as a quasi-1D current sheet. Effects such as changing magnetic field strength and plasma parameters due to the Earth's dipole field are not included. However, even with these limitations, the predictions give KAW amplitudes and Poynting flux that are testable by in situ satellite observations.

Magnetotail parameters used are $B=20$ nT, $n=0.1$ cm^{-3}, $T_i=1$ keV, *and* $T_e=300$ eV, which are typical conditions found in this region. The ion inertial length (d_i) and KAW wavelength using these parameters are 721 km and 1, 180 km, respectively, which are much smaller compared to the magnetotail scale lengths $20-30\,R_E$. Using the parallel wave speed and the damping frequency from the linear Vlasov calculation, we calculated how far a KAW will travel before attenuating to 10% of its initial amplitude. For different oblique propagation angles, we plot this distance versus $k\,d_s$ in Figure 7a. Reference lines are drawn for parallel propagation distances of $20R_E$, which would be sufficient for the KAW to propagate global magnetotail distances. While KAW with $k\,d_s\sim0.25\rightarrow k\,d_i\sim1$ will easily propagate these global distances, KAW with $k\,d_s\gg0.25$ would be expected to damp away well before that point.

We also estimate the change in Poynting flux strength as the KAWs propagate away from the x line using $S\approx S_x\approx B_z B'_z C_{Az} d_i/4\pi$ from Shay et al. (2011), where $B'_z=\partial B_z/\partial y\approx k\,B_z$. Using $B_z/B_{\rm up}\approx0.3$ and the parallel wave speed, in Figure 8 is shown the Poynting flux versus distance from the x line for selected wave numbers and propagation angles. Higher k values as expected begin with higher Poynting flux but show increased damping with distance. On the other hand, $k\,d_s\sim0.25$ shows almost no damping. The angle of propagation has a large effect for higher wave numbers.

Using the rough approximation from Shay et al. (2011) that the Poynting flux stays on the same magnetic flux tube and ignoring mode conversion and reflection, we estimate the Poynting flux in the ionosphere as $S_{\rm ion}\sim(B_{\rm ion}/B_{\rm lobe})S_{\rm lobe}\sim10^3 S_{\rm lobe}$. The minimum Poynting flux capable of creating white light aurora is estimated as 10^{-3} W/m^2, giving a white light threshold of 10^{-6} W/m^2 for Figure 8, which is drawn as a horizontal dotted line. We emphasize that this threshold is uncertain and should be viewed only as an order of magnitude estimate, as it does not include wave conversion and other effects associated with changing plasma conditions. Thus, for the angles presented, $k\,d_s\sim0.25\rightarrow k\,d_i\sim1$ has the potential to create white light aurora, but $k\,d_s\gg0.25$ is not expected to.

For the solar corona, we also estimate the distance a reconnection KAW could travel before B_z damps to 10% its original amplitude. Parameters used are $B=0.05$ T, $T_i=10^7$ K, $T_e=10^7$ K, and $n=3.0\times10^9$ cm^{-3}. Propagation distances are shown in Figure 7b. A typical flare loop has length 30–100 Mm that is $0.05-0.15\,R_\odot$. All KAW with $k\,d_s\sim0.02\rightarrow k\,d_i\sim1$ damp to 10% after propagating at most 1 order of magnitude less than a flare loop

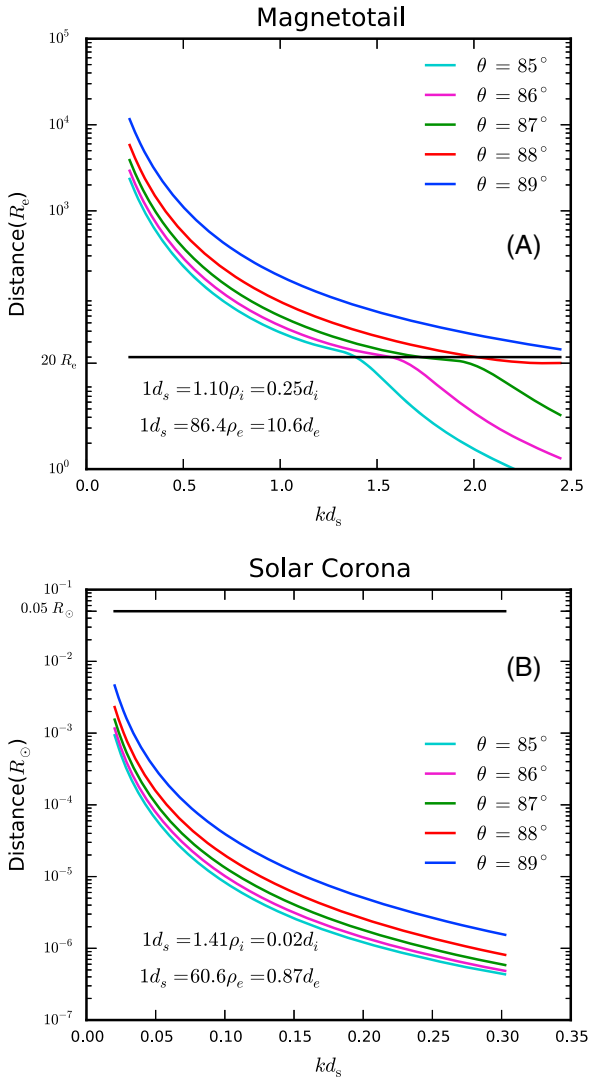

Figure 7. Distance traveled by reconnection KAW before it attenuates to 10% of its initial B_z amplitude for several oblique propagation angles θ. Conversion between fluid Larmor radius d_s, ion Larmor radius ρ_i, and ion inertial length d_i given in each panel. Note that this extrapolation assumes constant background plasma and field conditions. (a) Magnetotail parameters: KAWs with $k\,d_s \lesssim 1$ can propagate global magnetotail distances of 20 R_E (shown by black line). (b) Solar corona parameters: All KAWs damp before reaching about $10^{-3} R_\odot$, which is about 1 order of magnitude smaller than a typical flare loop length.

length. The reconnection KAW would not be expected to reach the photosphere and generate hard x-rays. Once again, we reiterate that these approximate should be viewed as an upper bound.

5. Conclusions

Using kinetic PIC simulations, we examine the attenuation of the Hall quadrupolar magnetic field structure during symmetric reconnection, which propagates as a kinetic Alfvén wave. This attenuation is consistent with predictions from linear Landau damping theory. Extrapolating to magnetotail parameters and using realistic mass ratio, KAWs with $k\,d_s \sim 0.25$ can propagate the global magnetotail distances on the order of 20 R_E without complete attenuation; therefore, these KAWs have the potential to create white light aurora.

There is a question of the validity of applying a simplistic 1-D wave analysis to the standing KAW structure associated with magnetic reconnection. Effects such as perpendicular wave propagation and/or wave dispersion could lead to an inaccurate estimation of the damping of the wave. Regarding perpendicular propagation, the inflow edge of the KAW boundary near the separatrices in Figure 1 remains quite sharp for large distances

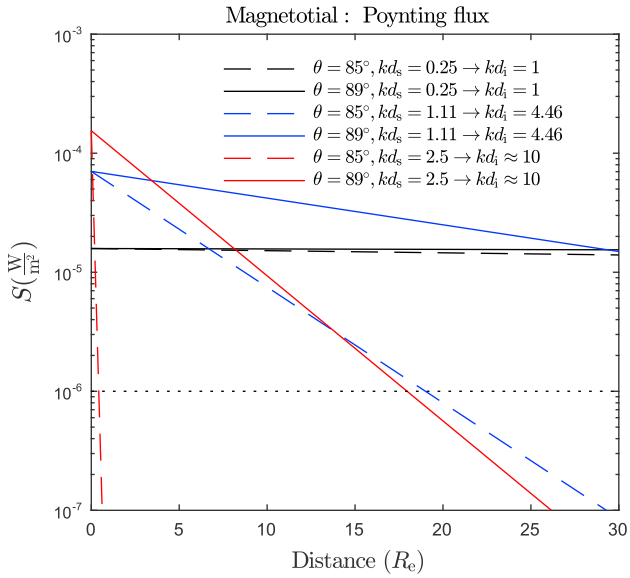

Figure 8. Strength of KAW Poynting flux S_x at different R_E distances from the reconnection x line. Angle of propagation of 85° and 89° is chosen for three distinct kd_s. Note that this extrapolation assumes constant background plasma and field conditions. The dotted line at 10^{-6} W/m^2 is a simplistic order of magnitude estimate of the threshold S that has the potential to create white light aurora, as described in the body of the text.

downstream of the x line; perpendicular spreading of the wave would be expected to blur this boundary. This lack of spreading is likely associated with the plasma inflowing velocity, which roughly balances the perpendicular propagation of the wave. Regarding wave dispersion, if dispersion were broadening the KAW, a traveling wave train associated (Coroniti, 1971) with dispersion would exist upstream of the separatrices. The key point, however, is that the linear Landau damping predictions match quite well with the 2-D nonlinear reconnection simulations. The applicability of linear damping to this systems appears quite robust, considering that this study uses both quasi-steady and time-varying analysis of the magnetic field lines, and also spans a range of plasma parameters and ion to electron mass ratio.

There are significant complications, however, that must be addressed in future studies before explicit predictions can be made about the role of these KAW in generating aurora and hard x-rays. As the waves approach the inner magnetosphere, the increasing magnetic strength is expected to enhance $k_\perp$, which likely would increase the damping. On the other hand, the amplitude of the wave can change due to mode conversion and reflection. This could, in fact, dominate over the effects of linear decay of the wave and thus may limit the scope of our predictions to a smaller tail region where most of the plasma background is uniform. Hence, the KAW propagation in the inner magnetosphere and auroral region will be the topic of future study. It is clear, however, that electron scale KAWs with $k\,d_s \gg 0.25$ will attenuate completely before reaching the inner magnetosphere. For the solar corona, on the other hand, all KAWs with $k\,d_s \gtrsim 0.02$ will damp long before reaching the photosphere.

Acknowledgments
This research was supported by NSF grants AGS-1219369, AGS-1219382, and AGS-1460130 and NASA grants NNX15AW58G and NNX08A083G-MMS IDS. Simulations and analysis were performed at the National Center for Atmospheric Research Computational and Information System Laboratory (NCAR-CISL) and at the National Energy Research Scientific Computing Center (NERSC). Archived simulation data are available upon request to the authors.

References

Angelopoulos, V., McFadden, J. P., Larson, D., Carlson, C. W., Mende, S. B., Frey, H., … Kepko, L. (2008). Tail reconnection triggering substorm onset. *Science*, *321*, 931–935.

Angelopoulos, V., McFadden, J. P., Larson, D., Carlson, C. W., Mende, S. B., Frey, H., … Kepko, L. (2009). Response to Comment on "Tail reconnection triggering substorm onset". *Science*, *324*, 1391.

Baker, D. N., Pulkkinen, T. I., Angelopoulos, V., Baumjohann, W., & McPherron, R. L. (1996). Neutral line model of substorms: Past results and present view. *Journal of Geophysical Research*, *101*, 12,975–13,010.

Chaston, C. C., Bonnell, J. W., Carlson, C. W., McFadden, J. P., Ergun, R. E., Strangeway, R. J., & Lund, E. J. (2004). Auroral ion acceleration in dispersive Alfvén waves. *Journal of Geophysical Research*, *109*, A04205. https://doi.org/10.1029/2003JA010053

Chaston, C. C., Johnson, J. R., Wilber, M., Acuna, M., Goldstein, M. L., & Reme, H. (2009). Kinetic Alfvén wave turbulence and transport through a reconnection diffusion region. *Physical Review Letters*, *102*(1), 015001.

Chaston, C. C., Phan, T. D., Bonnell, J. W., Mozer, F. S., Acuña, M., Goldstein, M. L., … Fazakerley, A. (2005). Drift-kinetic Alfvén waves observed near a reconnection X line in the Earth's magnetopause. *Physical Review Letters*, *95*(6), 065002.

Coroniti, F. V. (1971). Laminar wave-train structure of collisionless magnetic slow shocks. *Nuclear Fusion*, *11*, 261.

Dai, L. (2009). Wave dynamics in the geomagnetic tail (PhD thesis). University of Minnesota.

Damiano, P. A., Johnson, J. R., & Chaston, C. C. (2015). Ion temperature effects on magnetotail Alfvén wave propagation and electron energization. *Journal of Geophysical Research: Space Physics*, *120*, 5623–5632. https://doi.org/10.1002/2015JA021074

Damiano, P. A., Johnson, J. R., & Chaston, C. C. (2016). Ion gyroradius effects on particle trapping in kinetic Alfvén waves along auroral field lines. *Journal of Geophysical Research: Space Physics*, *121*, 10,831–10,844. https://doi.org/10.1002/2016JA022566

Fletcher, L., & Hudson, H. S. (2008). Impulsive phase flare energy transport by large-scale Alfvén waves and the electron acceleration problem. *Astrophysics Journal*, *675*, 1645–1655.

Gary, S. P. (1993). *Theory of space plasma microinstabilities, Cambridge Atmospheric and Space Science Series*. New York: Cambridge University Press.

Gershman, D. J., F-Viñas, A., Dorelli, J. C., Boardsen, S. A., Avanov, L. A., Bellan, P. M., … Burch, J. L. (2017). Wave-particle energy exchange directly observed in a kinetic Alfvén-branch wave. *Nature Communications*, *8*, 14719.

Keiling, A., Wygant, J. R., Cattell, C. A., Mozer, F. S., & Russell, C. T. (2003). The global morphology of wave Poynting flux: Powering the aurora. *Science*, *299*, 383–386.

Kepko, L., Spanswick, E., Angelopoulos, V., Donovan, E., McFadden, J., Glassmeier, K.-H., … Singer, H. J. (2009). Equatorward moving auroral signatures of a flow burst observed prior to auroral onset. *Geophysical Research Letters*, *36*, L24104. https://doi.org/10.1029/2009GL041476

Lapenta, G., Goldman, M. V., Newman, D. L., & Markidis, S. (2013). Propagation speed of rotation signals for field lines undergoing magnetic reconnection. *Physics of Plasma(1994-present)*, *20*, 102113.

Lui, A. T. Y. (1996). Current disruption in the Earth's magnetosphere: Observations and models. *Journal of Geophysical Research*, *101*, 13,067–13,088.

Lui, A. T. Y. (2009). Comment on "Tail reconnection triggering substorm onset". *Science*, *324*, 1391.

Lysak, R. L., & Lotko, W. (1996). On the kinetic dispersion relation for shear Alfvén waves. *Geophysical Research Letters*, *101*, 5085–5094.

Lysak, R. L., & Song, Y. (2011). Development of parallel electric fields at the plasma sheet boundary layer. *Journal of Geophysical Research*, *116*, A00K14. https://doi.org/10.1029/2010JA016424

Lysak, R. L., & Song, Y. (2004). Propagation of Alfvén waves at the plasma sheet boundary layer. In T. Pulkinnen & N. Ganushkina (Eds.), *Substorms 7: Proceedings of the 7th International Conference on Substorms* (81 pp.). Helsinki, Finland: Finnish Meteorological Institute.

Lysak, R. L., Song, Y., & Jones, T. W. (2009). Propagation of Alfvén waves in the magnetotail during substorms. *Annales Geophysicae*, *27*, 2237–2246.

Nishimura, Y., Lyons, L., Zou, S., Angelopoulos, V., & Mende, S. (2010). Substorm triggering by new plasma intrusion: THEMIS all-sky imager observations. *Journal of Geophysical Research*, *115*, A07222. https://doi.org/10.1029/2009JA015166

Rogers, B. N., Denton, R. E., Drake, J. F., & Shay, M. A. (2001). Role of dispersive waves in collisionless magnetic reconnection. *Physical Review Letters*, *87*(19), 195004.

Shay, M. A., Drake, J. F., Eastwood, J. P., & Phan, T. D. (2011). Super-Alfvénic propagation of substorm reconnection signatures and Poynting flux. *Physical Review Letters*, *107*(6), 065001.

Watt, C. E. J., & Rankin, R. (2009). Electron trapping in shear Alfvén waves that power the aurora. *Physical Review Letters*, *102*(4), 045002.

Watt, C. E. J., & Rankin, R. (2010). Do magnetospheric shear Alfvén waves generate sufficient electron energy flux to power the aurora? *Journal of Geophysical Research*, *115*, A07224. https://doi.org/10.1029/2009JA015185

Zeiler, A., Biskamp, D., Drake, J. F., Rogers, B. N., Shay, M. A., & Scholer, M. (2002). Three-dimensional particle simulations of collisionless magnetic reconnection. *Journal of Geophysical Research*, *107*, 1230. https://doi.org/doi:10.1029/2001JA000287